CrossMark

RESEARCH PAPER

Micro-PIV measurements of flows induced by rotating microparticles near a boundary

Jamel Ali[1] · Hoyeon Kim[2] · U. Kei Cheang[1] · Min Jun Kim[2]

Abstract We report on the hydrodynamics induced by single-digit micron-sized superparamagnetic particles rotating at low Reynolds number and analyze the resultant flow fields using microparticle image velocimetry (μPIV). Magnetic microparticles floating a few nanometers above a glass substrate, in an otherwise quiescent fluid, were actuated wirelessly using a rotating magnetic field controlled using two pairs of orthogonally positioned electromagnetic coils. A high-speed camera was used to sufficiently capture the motion of nanometer-sized seeding particles at 500 frames per second as well as track the rotation of microparticles. Data from μPIV are compared with the analytical solution for Stokes flow generated by a sphere in an infinite fluid and numerical simulations using finite element analysis. Two-dimensional velocity data obtained from stacks of planar flow fields at incremental depths for individual microparticles show non-symmetrical profiles that are an indication of increased viscous effects due to the boundary confining wall. Additionally, the flow fields generated by two particles, at various separation distances, are also analyzed. It is observed that as two synchronously rotating beads, of approximately equal diameter, are placed closed together, complex flows offset, superimpose, and merge into single, larger microvortices. We find that the flow fields generated by two physically bound microparticles, rotating as one unit, are well approximated by the flow generated by a single microparticle with twice the diameter.

1 Introduction

There is a long history of research on the behavior of active microparticles in fluidic environments, which dates as far back as the early twentieth century when small magnetic particles were first used to characterize the mechanical properties of biological fluids, such as the viscoelasticity of slime mold plasmodia (Heilbrunn 1956) and the cytoplasm of sea urchin eggs (Seifriz 1924). These early works were further developed in the 1950s by Crick and Hughes who established a basic theoretical framework for understanding the dynamics of microparticle behavior in external magnetic fields, as well as establishing new experimental techniques to apply external torques on magnetic particles (Crick and Hughes 1950). The pioneering advances by these researchers laid the foundation for the field of active microrheology, where particle displacements are correlated with rheological properties. Active microrheology has many advantages over traditional macroscale rheology methods, such as the ability to probe the mechanical responses of complex fluids and gels, which have heterogeneous properties that can vary depending on length scale. Over the past 20 years, due in part to new developments in colloidal engineering, rotating magnetic particles have been used to measure the mechanical properties of a number of complex fluids, such as butterfly saliva and alginate-based hydrogels (Nguyen and Anker 2014; Tokarev et al. 2013).

While microrheology has driven the investigation of rotating microparticles over the past century, there is currently a renewed interest in this topic due to new microfluidic applications. One such application is microscale

✉ Min Jun Kim
mjkim@lyle.smu.edu

[1] Department of Mechanical Engineering and Mechanics, Drexel University, Philadelphia, PA, USA

[2] Department of Mechanical Engineering, Southern Methodist University, Dallas, TX, USA

mixing and pumping, where arrays of rotating magnetic particles can efficiently manipulate complex fluids in low Reynolds number flows (Owen et al. 2013). Another relatively recent application of rotating magnetic particles is mask-free colloidal patterning through magnetohydrodynamic self-assembly (Grzybowski et al. 2000; Tierno et al. 2007; Yan et al. 2015). The patterns formed using this technique are the result of competing interactions between hydrodynamic vortex–vortex repulsion, which arise due to flows generated by microparticles, and attractive magnetic forces (Tretiakov et al. 2009). Once formed, these patterns have the potential to be used for several applications, including colloidal lithography. One of the newest and most promising applications of rotating microparticles is their use as microrobots and fluidic tweezers for non-contact micromanipulations. In this application, microparticles are both rotated and translated while ferrying objects. The microvortices generated by the rotational motion have been used to trap a variety of objects, including live bacteria (Petit et al. 2011; Ye et al. 2014; Ye and Sitti 2014).

There have been several theoretical papers on the subject of a rotating sphere in viscous fluids at rest, yet relatively few reports on the effect of boundaries (Chaoui and Feuillebois 2003; Goldman et al. 1967a, b; Roy and Damiano 2008). Furthermore, recent theoretical studies have shown the emergence of complex vortex dynamics between the flow fields generated by multiple plane-confined rotors, including the emergence of chaos (Lushi and Vlahovska 2015). These findings are worth exploring experimentally as reports of chaotic flows in low Reynolds number regime are still very sparse due the tendency of low Reynolds number flows to be linearly reversible. With so many applications, it is surprising that there is little literature on the emergent dynamics of multiple rotating particles in quiescent flow and even fewer experimental reports on the wall effects in these systems. Quantitative knowledge of these flow field dynamics can further advance the design of particle-based microfluidics. To experimentally examine these hydrodynamics here, we investigate the resultant flow phenomena generated by rotating microparticles. Using microparticle image velocimetry (μPIV) and computational fluid dynamics (CFD) simulations, quasi-steady-state time domains are investigated for rotating single-digit micrometer superparamagnetic particles. In addition, the sequential flow fields generated by two particles as they approach each other, to form dimers, are also analyzed. Based on the experimental measurements and numerical simulations, generated microvortices are analyzed both quantitative and qualitatively. The influence of particle size, boundary effects, and separation distance on generated flow is presented.

2 Materials and methods

2.1 Microfluidic system

Carboxylated magnetic microparticles (4 and 8 μm in diameter), consisting of superparamagnetic nanoparticles embedded in a polymer matrix (Bangs Laboratories), were used as active rotors. Stock magnetic particle solutions were diluted in DI water, containing 0.002 % of the nonionic surfactant Tween 20, to obtain a solution that was 0.001 % microparticle by weight; this dilution was used to lower the number of particle aggregates and limit flow field interactions between particles. Fluorescent seeding particles, 200 nm in diameter (FluoSpheres®, Ex:660/Em:680, Life Techn. Co.), were mixed with the dilute suspension of magnetic microparticles such that the final seeding concentration was approximately 0.2 mg/mL. Before each experiment, the working suspension containing both magnetic microparticles and fluorescent seeds was briefly mixed by vortexing. These particle suspensions were placed in borosilicate glass capillaries (inner dimensions 2.00 mm × 0.50 mm × 0.05 mm) that were sealed with grease (Fig. 1c). Within approximately one minute, the majority of the magnetic microparticles came to rest at the bottom of the container, due to a density mismatch with the surrounding fluid. To limit background flows, filled capillaries were allowed to equilibrate for 5 min before conducting experiments where approximately neutrally buoyant seeding particles were advected by the flow generated by rotating microparticles. The terminal velocity (unhindered) of the magnetic microparticles, with a density of 1.2 g/cm^3, was approximately 7 μm/s, for an 8-μm-diameter particle, and 2 μm/s, for a 4-μm-diameter particle. In addition, planes above particle(s) chosen for PIV analysis were observed to ensure that no other microparticles were in their proximity.

In order to exert an external torque on the magnetic microparticles, without inducing translational motion, experiments were conducted in a uniform rotational magnetic field generated by a custom-built approximate Helmholtz coil system. This system consisted of two pairs of orthogonally positioned copper coils connected to two power supplies (BOP 20-5 M, Kepco) that were controlled via a National Instruments data acquisition system (BNC-2110/PCI-6259) as previously reported (Cheang and Kim 2015). The coil system was fixed onto an inverted microscope (Leica DMIRB) with a motorized stage that was connected to a Photron FASTCAM SA3 high-speed complementary metal-oxide semiconductor (CMOS) camera (1024 × 1024 pixels and 12-bit). Filled capillaries were placed in the center of the coil system, where a uniform magnetic field of ~15 mT was generated. Magnetic field
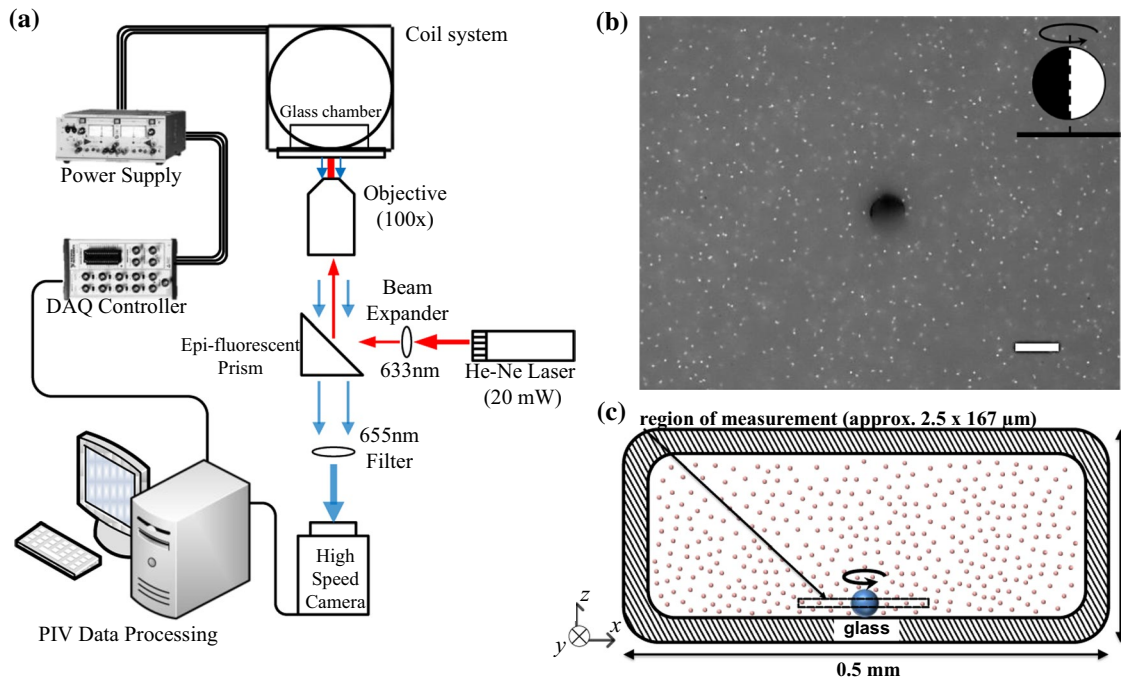
Fig. 1 **a** Schematic of the experimental system used for μPIV. **b** Typical florescence image observed during μPIV experiments: a half-coated magnetic microparticle, surrounded by 200-nm seeding particles, rotating on *top* of a glass substrate; *inset* is schematic representation of the rotation of the microparticle about an axis perpendicular to a surface normal (*scale bar* is 10 μm). **c** Cross-sectional schematic of the experimental glass chamber with the approximate region of measurement shown in *dotted lines*. Note that the scale is compressed in the horizontal direction

rotational frequency and orientation (clockwise/counterclockwise) were controlled via a custom LabVIEW program. To create a rotational field in the *xy* plane, coil pairs were set to generate sinusoidal signals that were out of phase by 90° such that the resultant magnetic field vector, **B**, can be written as:

$$\mathbf{B} = B \sin{(\Omega t)}\hat{\mathbf{i}} + B \cos{(\Omega t)}\hat{\mathbf{j}} \tag{1}$$

where Ω is the rotational frequency of the field, B is the magnitude of the magnetic field, and t is time.

The experimental chamber was exposed to the uniform rotational field for at least 30 s prior imaging, to ensure that the flow around the particles was fully developed.

2.2 Synchronous rotation of magnetic microparticles

To ensure that magnetic microparticles were rotating synchronously with the external magnetic field, we investigated their rotational behavior. Due to their isotropic geometry, it can be difficult to track spherical particles rotational motion; however, by non-uniformly coating particles with a thin layer of metal, their rotational rates can be accurately measured using microscopy (McNaughton et al. 2006). Using this approach, magnetic microparticles were coated with a thin, 100-nm, non-conformal hemispherical layer

of aluminum using thermal vapor deposition, resulting in half-coated Janus particles (see Fig. 1b). Videos, taken at 500 frames per second, of these Janus particles rotating with various external field frequencies, were analyzed for average rotational frequencies by applying a Fourier transform on their intensity fluctuations, as previously reported (Kinnunen et al. 2010). It was observed that microparticles rotated synchronously with a 15 mT external field until a critical frequency was reached, between 20 and 30 Hz (Fig. 2c), after which there was monotonic decrease in particle rotation with increasing external field frequency. It has been reported that this asynchronous rotation occurs when the phase lag between the dipole moment of a particle and the applied external field becomes larger than 90°, resulting in phase-slipping (McNaughton et al. 2006). To ensure synchronous rotation, all μPIV experiments were conducted with the external field frequency set well below the critical frequency, i.e., 10 Hz.

2.3 μPIV processing

The μPIV system consisted of a JDS Uniphase Corporation continuous-wave ($\lambda = 633$ nm) He–Ne laser, with a maximum beam power of 20 mW, that was used to excite fluorescent seeding particles (Fig. 1a, b). The emitted beam
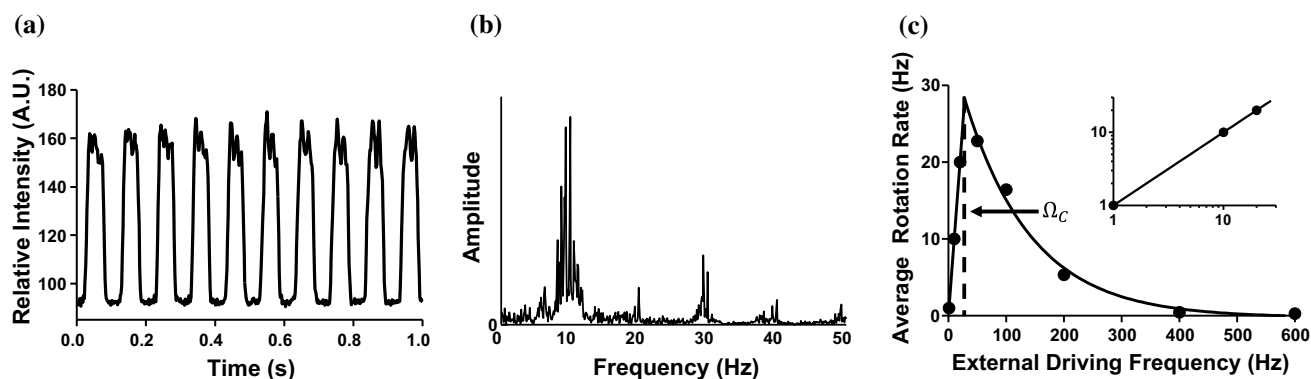
Fig. 2 Characterization of the magnetic responsiveness of superparamagnetic microparticles in a uniform 15 mT rotational field. **a** Intensity fluctuations of rotating Janus microparticles over time. **b** Fourier transform of (**a**), where the peak at 10 Hz represents the average rotational rate. **c** Average particle rotational rate at different driving frequencies, *inset* shows linear synchronous regime; the critical phase-slipping rate, Ω_C, occurs between 20 and 30 Hz

was focused through a cylindrical lens placed in front of a $10\times$ beam expander that was used to flood illuminate the sample chamber above a $100\times$ oil immersion objective lens. Particle images were captured by the high-speed CMOS camera. The CMOS chip had an image plane measuring 0.22×0.22 mm^2, where each square pixel had a side length of 17 µm, thus using a $100\times$ lens the size of a pixel on the recorded image plane was 0.17 µm. Due to the limited internal memory capacity of the camera (2 GB), all images were captured at a resolution of 768×768 pixels at an image acquisition rate of 500 frames per second for 4.89 s, corresponding to 2420 images. A representative single-frame image used for PIV analysis is shown in Fig. 1b; note that the image appears bright due to background fluorescence from out-of-focus seeding particles. Captured videos were analyzed, and time-averaged velocity vector flow fields were generated with commercial PIV software (DaVis 8.0). Vector fields were calculated using one pass of a 64×64 pixel interrogation window, followed by two passes of a 32×32 pixel interrogation window that had an overlap of 50 %. For each PIV time series, 3×3 smoothing was applied in vector post-processing.

In PIV, uncertainties in the experimental measurement of particle displacements determine the spatiotemporal accuracy at which velocity fields can be measured. To determine the minimum resolvable velocity changes, the root-mean-square (rms) error in velocity measurements was estimated as previously described (Kim et al. 2004). The rms velocity measurement error is given by:

$$\sigma_u = \frac{\sigma_{\Delta x}}{M_o \Delta t} \tag{2}$$

where $\sigma_{\Delta x}$ is the rms measurement error in determining a particles centroid displacement, M_o is the objective magnification, and Δt is the inter-frame recording time. Taking

$\sigma_{\Delta x}$ to be within 4 % of the recorded image diameter, this rms error can be written as a function of the optical image diameter prior being recorded on the pixel plane, d_e, and the resolution of the recording medium, d_r, which can be approximated as the pixel size (17 µm).

$$\sigma_{\Delta x} = 0.04 \left(d_e^2 + d_r^2 \right)^{1/2} \tag{3}$$

It has been determined (Raffel et al. 2013) that if captured particle images follow a Gaussian intensity profile and are diffraction-limited, d_e can be expressed as:

$$d_e^2 = M_o^2 d_p^2 + \left[2.44(1 + M_o) f^{\#} \lambda \right]^2 \tag{4}$$

where d_p is the diameter of the seeding particles (200 nm), and $f^{\#}$ is the relative aperture of the camera lens (0.4). From Eqs. (3) and (4), it was determined that a seeding particle would have an image plane diameter $\left(d_e^2 + d_r^2 \right)^{1/2}$ of 19 µm, meaning that a single-particle image occupies approximately 1.1 pixels, which near the ideal value of 1.5 for minimizing displacement measurement uncertainties (Raffel et al. 2013). From Eqs. (2) and (3), $\sigma_{\Delta x}$ and σ_u were determined to be 0.75 µm and 1.9 µm/s, respectively. The minimum resolvable velocity set by the rms error was found to be adequately small compared to flows generated by microparticles rotating at 10 Hz, which are on the order of 10^1 µm/s near their surface.

While most experiments were conducted with the focal plane fixed near the equatorial cross section of spinning microparticles, a set of experiments was also conducted at various focal planes to obtain velocity profiles at different z heights. To approximate the smallest increment that could be used for this experiment, the measurement depth of field was calculated. The measurement depth of µPIV can be defined as double the distance from the focal plane in
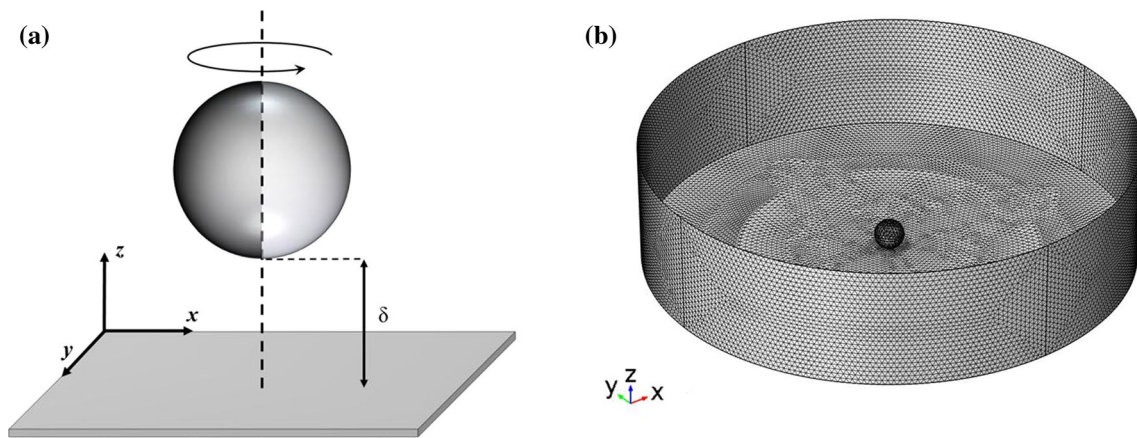
Fig. 3 **a** Schematic representation of microparticle rotating about an axis parallel to a surface normal, where δ is the distance between the bottom of the particle and underlying surface. **b** Meshed model constructed in COMSOL for numerical simulations

which the unfocused particle image no longer contributes to velocity measurement (Meinhart et al. 2000), which can be described by:

$$\delta z_m = \frac{3n\lambda}{NA^2} + \frac{2.16 d_p}{\tan\theta} + d_p \tag{5}$$

where n is the refractive index of the fluid in-between the sample chamber and objective lens (1.515 for oil), d_p is the seeding particle diameter, NA is the numerical aperture, and θ is the light collection angle, here 55.6°. From Eq. (5), the measurement depth was determined to be 2.47 μm, and thus, we limited z-directional flow field measurements to two micrometer increments.

2.4 Numerical simulations

The analytic solution for a neutrally buoyant sphere rotating in an otherwise quiescent infinite fluid was solved over a century ago (Jeffery 1915); however, in the present case where a particle, rotating about an axis parallel to the surface normal (Fig. 3a), is very close to the boundary, there currently exist no analytical solution. In this system, generated flow fields can interact with the boundary, leading to deviations from Stokes flow. Thus, to model the experimental system, steady-state flow fields were obtained through finite element computational modeling using commercial software (COMSOL Multiphysics, Stockholm, Sweden). Simulations were conducted to solve the incompressible form of the three-dimensional steady-state Stokes equations and mass continuity,

$$-\nabla p + \eta\nabla^2 \boldsymbol{u} = 0$$
$$\nabla \cdot \boldsymbol{u} = 0 \tag{6}$$

where p, η, and $\boldsymbol{u}$ represent the pressure, dynamic viscosity, and velocity vector field, respectively. The modeled

geometries featured 8- and 4-μm-diameter spheres positioned 100 nm above the surface inside of a 50-μm-diameter cylinder. We note that this model slightly deviates from the experimental system in that the particles in our experiments were not completely spherical, partly due to the hemispherical aluminum coating, and are in closer proximity to the substrate (approximately a few nanometers). In order to simulate the rotation of the spheres, a sliding wall boundary condition ($\boldsymbol{u} = \boldsymbol{u}_w$), where $\boldsymbol{u}_w$ is a predefined angular velocity vector, was applied to the surface of the spheres; no-slip boundary conditions ($\boldsymbol{u} = 0$) were applied to the walls of the cylindrical chamber. The properties of the fluid that surrounded the spheres were chosen to match those of water at 20 °C, i.e., ($\nu = 1.002$ mm^2/s). The computational domain consisted of 10^5–10^6 tetrahedral mesh elements, depending on the size and number of spheres used. All solutions were found to converge with residuals bellow 10^{-7}.

3 Results and discussion

3.1 Validation

In microfluidic environments, viscous forces dominate over inertial effects, and this relationship can be quantified through the Reynolds number. For rotational flow, the rotational Reynolds number is defined by the angular velocity, ω, kinematic viscosity, ν, and a characteristic length, R.

$$Re = \frac{\omega R^2}{\nu} \tag{7}$$

For microspheres with diameters around 10 μm rotating at 10 Hz, the rotational Reynolds number is on the order of 10^{-9}. The flows generated by these particles are clearly in the low Reynolds number regime. In order to confirm
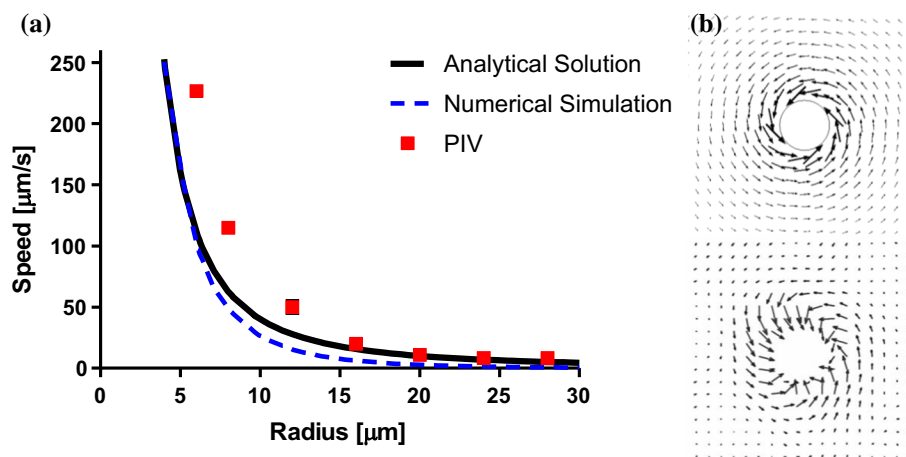
(a)

(b)

Fig. 4 Comparison between analytical solution, μPIV measurements, and finite element simulation, at a vertical position of 4 μm above the glass substrate, for μPIV validation. **a** The *solid line* represents the analytic solution for a sphere, 8 μm in diameter, rotating in an infinite fluid. The *dashed line* represents the results obtained from a finite element simulation for an 8-μm sphere rotating near a boundary. The *squares* are from μPIV measurements along a *radial line*, *r*, with fixed angle, *θ*. **b** Characteristic flows observed at the equatorial cross-sectional plane of the microsphere obtained from finite element simulation (*top*) and μPIV (*bottom*)

that μPIV data were in general agreement with predicted by theory, experimental data for a rotating particle were compared to both analytical and numerical solutions. For a sphere rotating at low Reynolds number, the analytical solution for the azimuthal velocity, v_φ, is given by:

$$\frac{v_\varphi}{\omega R \sin \theta} = \left(\frac{R}{r} \right)^2 \tag{8}$$

where θ, R, and r are the polar angle, sphere radius, and radial distance from the center of a sphere, respectively (Bird et al. 1987). A comparison of the analytical solution, numerical simulation, and experimental results for an 8-μm bead rotating at 10 Hz are shown in Fig. 4a. It is important to note that the analytical solution assumes that the sphere is in an otherwise quiescent, infinite expanse of fluid, while in the experimental system the microparticles are resting just above a glass surface in a finite fluid volume. Also, note that due to electrostatic repulsion between the negatively charged carboxylated microparticle surface and the negatively charged glass surface, microparticles are not in direct contact with the substrate, but are floating a few nanometers above the surface (Tierno et al. 2007); however, to use the continuum model for numerical simulations, i.e., Knudsen number $<10^{-3}$, particles were set one micron above the surface. While the main difference between the experiment and idealized case is the presence of a solid boundary near the sphere, the analytical solution generally agrees with what is seen experimentally; the flow field exponentially decays as the radial distance from sphere increases. Comparing the numerical and analytical

solutions, the finite element analysis yielded a flow field that decays slightly faster than that of the analytical solution, $1/r^2$. Fitting the numerical solution with a power-law model, the flow field decays at a rate of $1/r^{2.06}$. The velocity field determined from μPIV data is overall higher than the numerical simulation, decaying at a slightly slower rate of $1/r^{1.72}$. This result is surprising as the increased viscous effects of the underling wall should cause a sharper drop in flow velocity than predicted from the analytical solution of an unbounded sphere. Also, while μPIV measurements far from the microparticle are in agreement with theory, measurements taken closer appear to be offset from what is predicted. These discrepancies are likely due to measurement errors. One possible source of error arises from low and non-uniform seeding particle densities near the particle surface, caused by electrostatic effects and 'slip' between the fluid and rotating seeding particles, decreasing spatial resolution (Li and Yoda 2008). Another source of error can be attributed to the highly curved flow field, similar to that of Lamb–Oseen vortices, which can significantly distort PIV measurements (Scharnowski and Kahler 2013). This bias error due to displacement vectors which are similar in magnitude to the microparticle curvature may be corrected by using a second-order shift vector, and its gradient, on the ensemble-averaged correlation (Scharnowski and Kahler 2013). However, while significant differences exist between theory and experiment close to the surface of the microparticle, the overall flow profile is still comparable to that predicted from the analytical solution and numerical simulation and shows that these flows are rotationally symmetric.

3.2 Mapping 3D flows

While µPIV is typically limited to mapping flows on a single plane, insight into three-dimensional flow profiles can be obtained by taking a series of two-dimensional flows at a series of heights, z. Using this method, a series of flow fields were obtained for both 4- and 8-µm-diameter microparticles, rotating at 10 Hz, in 2-µm increments staring from a focal plane close to glass substrate surface. In Fig. 5a, the flow field profiles of azimuthal velocity, at a series of heights, reveal that the magnitude of the flow is greatest near the equator of the microparticle and diminish as radial distance from the equator increases; this follows what is predicted from the analytical solution. Furthermore, from the profiles of 8-µm microparticles, it appears that the maximum flow occurs approximately two microns above the equatorial plane. This can be explained by the increased

rotational drag forces that arise due to the presence of a confining wall. It is clear from Fig. 5a that measured flow fields below the equatorial planes of both microspheres are significantly smaller than those mirrored on the opposite side of the equatorial plane, which are subjected to lessened wall-induced drag forces. The neighboring boundary breaks the axial symmetry of the rotational flow field, which is apparent due to strong viscous effects that are a function of the low rotational Reynolds number and small microparticle-wall gap widths (Liu and Prosperetti 2010). This phenomenon has been reported theoretically and experimentally quantified by using optical traps to apply a known torque on microparticles and then measuring the resultant rotational rate (Leach et al. 2009).

Characteristic flow patterns generated by rotating microparticles were observed through qualitative streamline visualization, as shown in Fig. 5b. Images were obtained by
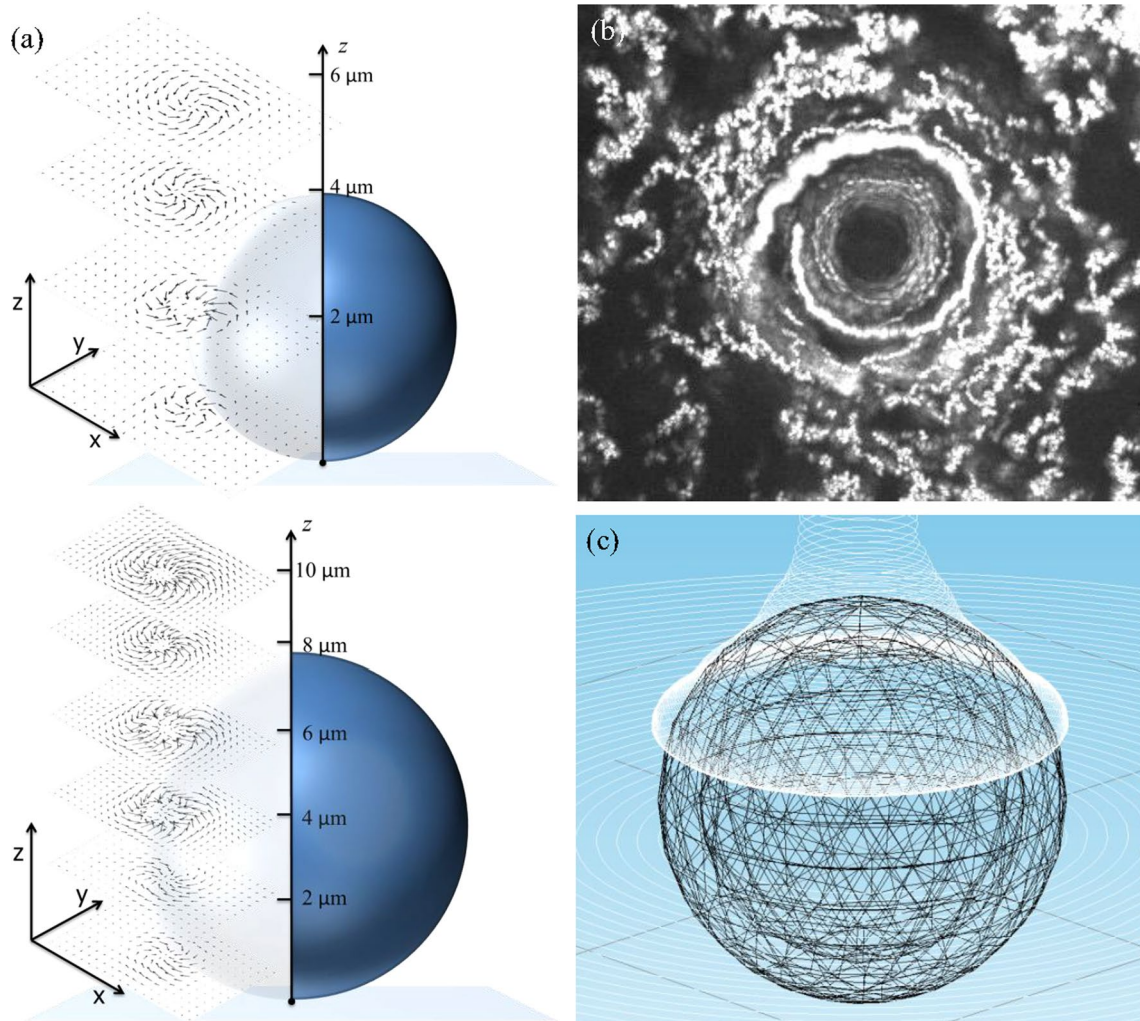

Fig. 5 a Characteristic vector flow fields observed at various cross sections for 4-µm (*top*) and 8-µm (*bottom*)-diameter microparticles rotating synchronously at 10 Hz. **b** Qualitative flow visualization of stead-state streamlines formed by digital averaging 100 sequential images acquired at 100 Hz. **c** Side view of the streamlines obtained from finite element simulation of 8-µm bead rotating near a boundary

digitally averaging a sequence of 100 consecutive frames. The size and shape of the formed microvortices, centered around the microparticles, are clearly observed from the formed streamlines, which are distinct from seeding particles undergoing thermally driven fluctuations. Visualization of the three-dimensional streamlines from numerical simulation, as shown in Fig. 5c, reveals that flow is pulled toward the poles of the sphere, toward the equator, where fluid then follows mainly circumferential paths around the sphere. It is also important to note that the flows at the two poles are unequal, with poleward flow on the wall side being retarded due to increased viscous drag.

3.3 Flow fields of rotating particles with various separation distances

In addition to investigating the flow fields generated by isolated microparticles, velocity profiles of two neighboring rotating particles were also analyzed. When two or more microparticles are actuated at low rotational frequencies and have relatively large inter-particle spacing, strong viscous forces limit hydrodynamic interactions between generated flows. However, as the separation distance between active rotors decreases, flow fields begin to interact, leading to hydrodynamic coupling of flows. We used µPIV to obtain the flow fields for pairs of 4-µm-diameter microparticles, rotating in phase, at a series of different approximant separating distances: 40, 20, 10, and 0 µm. Figure 6 shows both the results from µPIV and numerical simulation. Comparing the results, there is a clear difference between the experimental and numerical data, especially near the particle surface, where in the µPIV data a region of low velocity flow near the surface of the microparticle is observed. We attribute the deviation between µPIV and numerical simulation to distortion in PIV measurements, due to the highly curved flow field, and the other measurement errors previously discussed in Sect. 3.1. However, even though there are distortions in the PIV measurements, bulk flow field interactions can still be distinguished. When microparticles were separated by large distances, approximately ten times the diameter of a single microparticle, their generated microvortices are essentially isolated and no discernable hydrodynamic interactions are apparent (Fig. 6a). As the separation distance becomes smaller, approximately half the distance of the previous case, while the generated microvortices remain distinct for each microparticle, their flows fields begin to interact, and the formation of a separatrix or stagnation point can be observed (Fig. 6b); in both the numerical simulation and µPIV plot, there is evidence that the flow field sharply decreases to zero in the region directly in-between the rotating microparticles. While a stagnation point is readily apparent in the numerical simulation of Fig. 6b, in the µPIV results, there is also

some indication of stagnation, as regions of low flow, represented by regions of dark blue/black in the heat map, are visible between the two particles. At an even smaller inter-particle spacing, individual microvortices are less distinct as they become hydrodynamically coupled and begin to form one coherent structure. From the numerical simulation, at the midpoint between the particles, it is clear that the flow reaches a minimum value (see Fig. 6c). However, in the µPIV results this local flow minimum (i.e., stagnation point) is not readily apparent; this can be attributed to the limited spatial resolution of the measurement along with the measurement errors previously discussed. Finally, when two microparticles become physically attached and rotate as one object (Fig. 6d), only a single microvortice is apparent. Furthermore, the previously observed separatrix is absent. Note that in Fig. 6d the numerical simulation is of a single 8-µm-diameter particle, while the µPIV result is of two 4-µm microparticles that have magnetically bonded and are rotating as one about their combined centroid. From these results, it appears that geometric differences between a dimer, i.e., two joined particles, and a single particle with twice the diameter do not significantly differ in the overall flow they generate and that the flows of a dimer can be closely approximated by the flow generated by a single larger particle.

In these experiments, except for the case of rotating dimers (Fig. 6d), microparticles were rotated in place; particles did not co-rotate. As the magnetic microparticles became in close proximity (within 5 µm), the particles were observed to co-rotate in orbit around each other, due to magnetohydrodynamic interactions. Analysis of particles undergoing co-rotation was omitted from analysis due to two main reasons: (1) co-rotation was non-periodic and (2) separation distances between particles rapidly changed, as magnetic attraction overwhelmed vortex–vortex repulsion, resulting in translational motion that brought particles together and made time-resolved µPIV measurements infeasible.

4 Conclusion

Despite the growing number of microfluidic applications of rotating microparticles, there has been relatively little work done so far in terms of measuring the flow fields that they generate. However, by being able to both visualize and quantitatively measure rotational microflow field dynamics, the design of particle-based microfluidics can be further advanced. In this paper, we have presented µPIV measurements of two-dimensional low Reynolds number rotational flows near a boundary. Although the rotational microparticle systems analyzed have relatively simple geometries, the emergence of complex flows, with rich
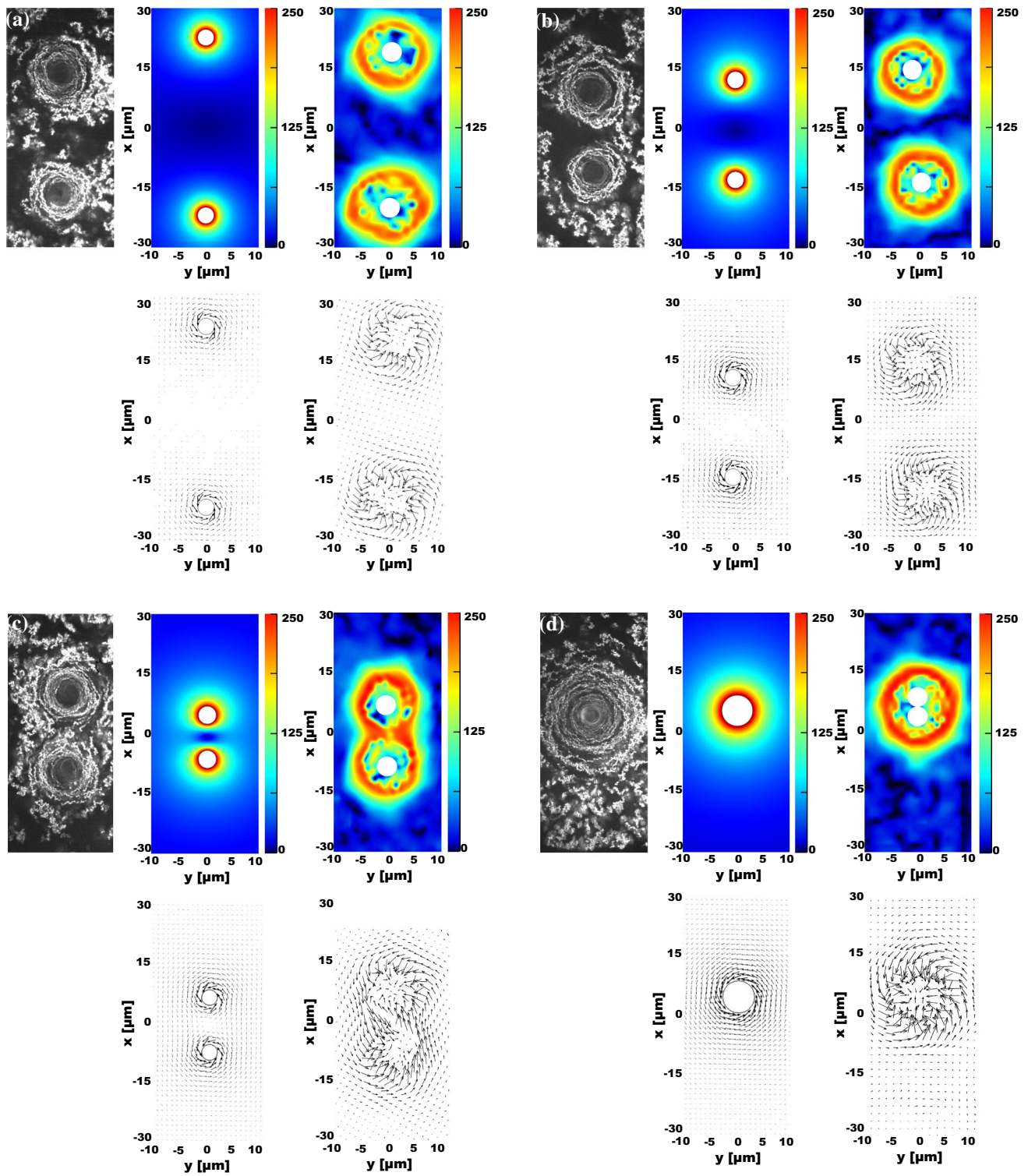
Fig. 6 From *left* to *right*, streamline visualization, finite element simulation, and μPIV results for the azimuthal velocity two 4-μm-diameter beads, rotating at 10 Hz, spaced apart at approximately **a** 40 μm, **b** 20 μm, **c** 10 μm, and **d** 0 μm. Vector fields correspond to the above simulation and μPIV plots, respectively. The units for the color coding are in μm/s. Note that in **d** the finite element simulation is of a single 8-μm sphere rotating at 10 Hz, and the corresponding μPIV result is of two joined 4-μm particles rotating at the same speed

dynamics, was observed. To validate the experimental system, μPIV results were compared with the both analytical and numerical solutions for perfect sphere rotation. While the μPIV results followed a general power-law drop off in velocity as radial distance from the microsphere increased, the drop in velocity was found to decrease at a slower rate than predicted. This result is surprising, as the increased viscous effects of the underling wall should cause a sharper drop in flow velocity than predicted from the analytical solution. This discrepancy between theory and experiment is most likely due to PIV measurement errors that are associated with non-ideal seeding particle distributions near the microparticle surface and significant streamline curvature. Yet, while the magnitudes of μPIV and the numerical simulation do not exactly match, the vector fields of the two flows are very similar. Using μPIV, stacks of two-dimensional flows were constructed and revealed that the increased viscous effects near the confining wall shift the maximum flow velocity above the equator of the microparticle. Finally, analyzing the flows generated by two same size rotating microparticles separated at a series of distances, it was observed that at a critical separation distance the microvortices begin to hydrodynamically couple, creating regions were flow fields superimpose and offset, until the two particles joint together to generate a single microvortice which agrees well the theoretical and experimental flow a single microparticles with twice the diameter. Complex vortex–vortex interactions due to competing repulsive hydrodynamics and attractive magnetic forces were unable to be resolved using time-averaged μPIV; however, by analyzing particles separated by distances sufficiently long enough that magnetic dipole attraction between microparticles was insignificant, purely hydrodynamic vortex–vortex interactions were observed. These results help in our understanding of the microhydrodynamics of active rotors, which we hope to extend in the future with μPIV measurements of flows generated by multiple microrotors.

References

Bird RB, Armstrong RC, Hassager O (1987) Dynamics of polymeric liquids. Volume 1: fluid mechanics. A Wiley-Interscience Publication, Wiley: New York

Chaoui M, Feuillebois F (2003) Creeping flow around a sphere in a shear flow close to a wall. Q J Mech Appl Math 56:381–410

Cheang UK, Kim MJ (2015) Self-assembly of robotic micro- and nanoswimmers using magnetic nanoparticles. J Nanopart Res 17:1–11

Crick FHC, Hughes AFW (1950) The physical properties of cytoplasm. Exp Cell Res 1:37–80

Goldman A, Cox R, Brenner H (1967a) Slow viscous motion of a sphere parallel to a plane wall: II Couette flow. Chem Eng Sci 22:653–660

Goldman A, Cox RG, Brenner H (1967b) Slow viscous motion of a sphere parallel to a plane wall: I motion through a quiescent fluid. Chem Eng Sci 22:637–651

Grzybowski BA, Stone HA, Whitesides GM (2000) Dynamic self-assembly of magnetized, millimetre-sized objects rotating at a liquid–air interface. Nature 405:1033–1036

Heilbrunn LV (1956) The dynamics of living protoplasm. Academic Press, New York

Jeffery G (1915) On the steady rotation of a solid of revolution in a viscous fluid. Proc Lond Math Soc 2:327–338

Kim MJ, Kim MMJ, Bird JC, Park J, Powers TR, Breuer KS (2004) Particle image velocimetry experiments on a macro-scale model for bacterial flagellar bundling. Exp Fluids 37:782–788

Kinnunen P, Sinn I, McNaughton BH, Kopelman R (2010) High frequency asynchronous magnetic bead rotation for improved biosensors. Appl Phys Lett 97:223701

Leach J, Mushfique H, Keen S, Di Leonardo R, Ruocco G, Cooper JM, Padgett MJ (2009) Comparison of Faxen's correction for a microsphere translating or rotating near a surface. Phys Rev E 79:026301

Li HF, Yoda M (2008) Multilayer nano-particle image velocimetry (MnPIV) in microscale Poiseuille flows. Meas Sci Technol 19:075402

Liu QL, Prosperetti A (2010) Wall effects on a rotating sphere. J Fluid Mech 657:1–21

Lushi E, Vlahovska PM (2015) Periodic and chaotic orbits of plane-confined micro-rotors in creeping flows. J Nonlinear Sci 25:1111–1123

McNaughton BH, Kehbein KA, Anker JN, Kopelman R (2006) Sudden breakdown in linear response of a rotationally driven magnetic microparticle and application to physical and chemical microsensing. J Phys Chem B 110:18958–18964

Meinhart CD, Wereley ST, Gray MHB (2000) Volume illumination for two-dimensional particle image velocimetry. Meas Sci Technol 11:809–814

Nguyen KVT, Anker JN (2014) Detecting de-gelation through tissue using magnetically modulated optical nanoprobes (MagMOONs). Sens Actuators B-Chem 205:313–321

Owen D, Mao WB, Alexeev A, Cannon JL, Hesketh PJ (2013) Microbeads for sampling and mixing in a complex sample. Micromachines 4:103–115

Petit T, Zhang L, Peyer KE, Kratochvil BE, Nelson BJ (2011) Selective trapping and manipulation of microscale objects using mobile microvortices. Nano Lett 12:156–160

Raffel M, Willert CE, Kompenhans J (2013) Particle image velocimetry: a practical guide. Springer, New York

Roy BC, Damiano ER (2008) On the motion of a porous sphere in a Stokes flow parallel to a planar confining boundary. J Fluid Mech 606:75–104

Scharnowski S, Kahler CJ (2013) On the effect of curved streamlines on the accuracy of PIV vector fields. Exp Fluids 54:1–11

Seifriz W (1924) An elastic value of protoplasm, with further observations on the viscosity of protoplasm. J Exp Biol 2:1–11

Tierno P, Muruganathan R, Fischer TM (2007) Viscoelasticity of dynamically self-assembled paramagnetic colloidal clusters. Phys Rev Lett 98:028301

Tokarev A, Kaufman B, Gu Y, Andrukh T, Adler PH, Kornev KG (2013) Probing viscosity of nanoliter droplets of butterfly saliva by magnetic rotational spectroscopy. Appl Phys Lett 102:033701

Tretiakov KV, Bishop KJM, Grzybowski BA (2009) The dependence between forces and dissipation rates mediating dynamic self-assembly. Soft Matter 5:1279–1284

Yan J, Bae SC, Granick S (2015) Colloidal superstructures programmed into magnetic janus particles. Adv Mater 27:874–879

Ye Z, Sitti M (2014) Dynamic trapping and two-dimensional transport of swimming microorganisms using a rotating magnetic micro-robot. Lab Chip 14:2177–2182

Ye Z, Edington C, Russell AJ, Sitti M (2014) Versatile non-contact micro-manipulation method using rotational flows locally induced by magnetic microrobots. Paper presented at the IEEE/ASME international conference on advanced intelligent mechatronics, 8 July 2014